Energy Transport in ASDEX in Relation to Theoretical and Semi-empirical Transport Coefficients

Otto Gruber, Reinhard Wunderlich,
Karl Lackner, Wolfgang Schneider

IPP

MAX-PLANCK-INSTITUT FÜR PLASMAPHYSIK

8046 GARCHING BEI MÜNCHEN

MAX-PLANCK-INSTITUT FÜR PLASMAPHYSIK

GARCHING BEI MÜNCHEN

Energy Transport in ASDEX in Relation to
Theoretical and Semi-empirical Transport Coefficients

Otto Gruber, Reinhard Wunderlich,
Karl Lackner, Wolfgang Schneider

IPP 5/29   September 1989

Energy Transport in ASDEX in Relation to Theoretical and Semi-empirical Transport Coefficients

O. Gruber, R. Wunderlich, K.Lackner, W. Schneider

Max-Planck Institut für Plasmaphysik
Euratom Association, D-8046 Garching

Abstract

A comparison of measurements with theoretically predicted energy transport coefficients has been done for Ohmic and NBI-heated discharges using both analysis and simulation codes .

The contribution of strong electrostatic turbulence given by the η_i-driven modes to the ion heat conductivity is very successful in explaining the observed response of confinement to density profile changes and is found to be even in good *quantitative* agreement.

Regarding the electron branch, a combination of trapped electron driven turbulence and resistive ballooning modes might be a promising model to explain both the correct power and density dependence of confinement time, and the observed radial dependence of the electron heat conductivity.

1.Introduction

A comparison of measurements with theoretically predicted energy transport coefficients can proceed basically along three lines:

(1) One can carry through a detailed analysis of the energy flows and temperature profiles using a code like TRANSP /1/. In this case the primary result consists in radial profiles of conductive heat fluxes, which can then be compared with those predicted by models using the given plasma parameters and their gradients.

(2) Simulation calculations can be performed for actual, well documented discharges using fully specified transport coefficients. The comparison with the experiments consists then primarily in a comparison of the measured and the predicted temperature profiles and the time-traces of characteristic global discharge parameters (like, in particular, the total kinetic energy of the species W_e, W_i or β_{pol}) .

(3) Series of simulation calculations can be performed for varying macroscopic parameters (e.g. I_p, $\bar{n}_e$, P_{tot}), not necessarily corresponding to actually carried out discharges. A large data base exists for most devices describing the variation of the global energy confinement time τ_E. The variation of τ_E in such scans can often not be correctly inferred from inspection of the local

transport coefficients, as deposition effects, sawteeth, or changes in the relative importance of different transport channels might mask the simple diffusivity trends.

In this report we described results of all three analyses approaches to purely Ohmic heating and to NBI-heated discharges in the L-regime. In the calculations presented we have paid little attention to the actual physics of particle transport. This is justified only in the spirit of an analysis closely orienting itself on existing experimental data, where it can be argued that the consequences of particle onto energy transport can only arise through the density profiles or the convective fluxes. In a TRANSP-type analysis the correctness of these is a priori ensured. For the simulations using the BALDUR-code /2/ we have chosen a particle transport model (applied also for the impurities) of the form

$$\Gamma_p = - D_p \frac{\partial n_e}{\partial r} + v_r \cdot n_e$$

with $v_r = - c_v (\gamma + 1) D_p (r/a)^\gamma /a$, and $D_p = c_p \chi_e$, using values of c_p, c_v and γ leading to approximately correct particle density profiles. Over the source-free region, the actual value of D_p will have no effect on the stationary density profile, but will of course determine its rate of change during dynamic phases, and its dependence on particle sources, like pellets or NBI. A feedback-system, acting on the hydrogen gas puff was used in the simulations to make them track the experimentally measured $\overline{n}_e(t)$ curves.

We have considered, either alternatively or in parallel the following contributions to electron and ion transport (the actual expressions used, including all numerical constants are given in appendix A):

(1) dissipative and collisionless trapped electron modes (TEM) /3/ using the expressions given by Waltz et. al. /4/.

(2) the semi-empirical model of Rebut et al. /5/ in different formulations. Results presented here use the formulas given in /6/.

(3) resistive ballooning modes using the neoclassical corrections and the formulas given by Callen et al./7/. (The formulation given in the original paper /8/ yields for ASDEX Ohmic and L-mode conditions χ_e-values always by one or two orders of magnitude too small).

(4) Becker's empirical expressions for χ_e in the form derived by using the dimensional constraints to fix the major radius dependence which obviously cannot be derived from ASDEX data alone /9/.

(5) Rogister's trapped electron mode model /10/

(6) neoclassical ion heat conduction including the corrections given in the papers by Chang-Hinton /11,12/.

(7) η_i-modes. We have used three alternative formulations, due to Mattor and Diamond /13/, Dominguez and Waltz/4/ and a combination of the expressions of Ref./14/ and /13/ proposed by Ross/15 /. In all cases we have included the corrections due to Romanelli /16/ to keep transport finite in the limit $\nabla n \rightarrow 0$.

In addition to the models given above we have sometimes added in the simulations a contribution

$$\chi_e = \frac{10^{19}}{n_e} \quad ..... \text{ (SI units)}$$

corresponding to 0.2 × Alcator-Intor. This served in some models - where transport should vanish *before* violation of a certain threshold criterium (e.g. Rogister's model) - as a *seed* value. In other cases (notably the trapped electron mode model as in item 1) this provided for a better approximation for the outer plasma layers as the first-principle model tested gave an obviously wrong variation of χ_e over the cross-section. As we wanted to test *strictly local* transport models we refrained form using explicit global constraints (as suggested in Ref. /17/) to adjust the profiles.

A further transport contribution was used to simulate in a time averaged sense the action of sawteeth: χ_e (and due to the explicit linkage used in our calculations also D_p and v_r) were augmented by a term

$$\chi_{eq1} = 0.4 \times \frac{\left(\frac{1-q^2}{q+q^2}\right)^2}{1 + \left(\frac{1-q^2}{q+q^2}\right)^2} \times D_{Bohm}$$

Some of the above transport models do not fit well into the numerical scheme used in the BALDUR-code and required particular adjustments. These are briefly described in appendix B of this report.

In principle one could carry out simulations with all possible combinations of ion and electron heat transport models. To get a uniform comparison of the electron heat transport models, we have combined each of them with an ion heat diffusivity enhanced three times above the neoclassical (Chang-Hinton) value χ_{CH} following ref. /11/. For the case of TEM electron transport we permutated through four different ion transport models (3 × χ_{CH}, and combinations of 1 × χ_{CH} with all three η_i-based models described above). Rebut's model was tested in two forms (1) only as an electron transport model (in combination with 3 × χ_{CH}) and (2) in the form containing a prescription for both electron and ion transport.

2. TRANSPort Analysis of an L-regime Discharge

For a detailed analysis and simulation of a discharge in terms of all the alternative transport models mentioned in the introduction, we singled out the well-documented ASDEX-shot nr. 17529. Time-traces of the global discharge parameters plasma current (I_p), loop-voltage (U_L), line average electron density through a mid-plane chord ($\overline{n}_e$), total radiated power(P_{rad}) are given in Fig.1, together with the time windows during which H^0-beams with 40kV energy in the main component and total powers (at the port) of 1.35 and 1.7 MW respectively were applied. The discharge was in a deuterium background gas, the main field (B_t)

was 2.3 T, and the plateau plasma current of 440 kA corresponds to an engineering q at the boundary ($q_a = (2\pi a^2 B_t)/(\mu_o I_p R)$; a, R..minor and major discharge radius) of 2.5. Fig.2 shows the energy confinement time τ_E, as derived from the total plasma energy, for the time interval 1.05 to 1.65 seconds, which includes the injection heated phase.

Diagnostic signals used to establish the energy balance and to carry out the comparison with the simulation results (and, where containing redundancies, to assess the consistency of the measurements) were provided by a 60Hz YAG-laser Thomson scattering system for the electron temperature and density $T_e(r)$ and $n_e(r)$, ECE measurements of T_e, passive CX neutral analyzers for the ion temperature profiles $T_i(r)$, neutron fluxes, 3 channels of a HCN interferometer for electron line densities, bolometers and soft X-rays for impurity content and radiation power and electromagnetic measurements giving U_L and the poloidal β (from diamagnetic loops as β_{dia} and in the form of the equilibrium parameter $\beta_{equ} + l_i/2$ from poloidal field and flux measurements). The discharge had low total radiated power (inside the seperatrix region less than 25% of the total input power are radiated during the 1.35 MW injection phase analyzed in the following). Z_{eff} as determined from U_L and the temperature profile under assumption of neoclassical parallel electrical conductivity was 1.2 during the Ohmic and 1.3 during the L-mode phase.

The discharge was first subjected to a TRANSP analysis and the temporal variation of the different power input and loss channels, evaluated at $r = 2a/3$ are given in Figs.3a,b. Fig.3c gives the resulting "effective" ion and electron heat diffusivities, defined through $\chi_k = -q_{h,k}/(\partial T_k/\partial r)$ at the same reference location. This analysis also reveals that the electron -ion coupling is relatively weak during the L-mode phase allowing a good separation between the ion and electron transport channels.

The simulation calculations were carried out for the Ohmic and the 1.35MW NBI-heating phase. The Ohmic phase will be discussed in connection with the power scan carried through in section 4. The detailed analysis of the profiles here and their comparison with simulations in chapter 3 will concentrate on the stationary L-mode phase represented in this discharge by the NBI-heated state at t = 1.29sec. For this instance we show in Fig. 4a-c radial profiles of the measured plasma parameters and the computed results of the TRANSP code. In the form the latter is used by us it requires specification of a ion heat transport model. We show the resulting ion temperature and conductivity profiles (Fig.4a and 4c) under the two assumptions (1) $\chi_i = \chi_{CH}$ and (2) $\chi_i = \chi_{CH} + \chi_{\eta i}$ (with the latter taken from ref./13/, multiplied by a factor 1.6) revealing a clearly much improved fit for the latter case (see also Ref /18/).

The effective electron heat diffusivity profiles derived by this analysis are compared in Fig. 5 with the theoretical predictions of the different model expressions evaluated for the measured local plasma parameters. This procedure leads to systematically larger discrepancies between

derived and predicted χ_e-values than appear in the simulation calculations of the next section. This stems from the nonlinearities in the theoretical expressions and the possibility of the temperature profiles in the simulation calculations to adjust to them. The qualitative tendencies observed, however, are the same in both cases and will be discussed in the context of the simulations described in the sections 3 and 4.

3. BALDUR Simulations of an L-regime Discharge

For this discharge #17529 we have also carried out BALDUR simulation calculation with the transport models mentioned in the introduction and specified in appendix A. The following comparison with the measurements and the derived results of section 2 will primarily concern the profiles of electron and ion temperature and of electron heat conductivity, and the global energy confinement times based on the total particle energy content.

To produce approximately the correct radiative losses and Z_{eff} we adjusted in the simulations an impurity inflow of carbon and iron, yielding a Z_{eff} of 1.25 and a radiated power fraction of 25% at the reference time instant of t = 1.29. The ratio between carbon and iron densities was kept nearly constant in all runs at 10:1. The parameters of the hydrogen particle and impurity transport model were chosen throughout the discharge as c_p = 0.35, c_v = 0.4, γ = 1.5, yielding (fairly independent of the model for χ_e) at the reference time the profiles of electron and impurity densities shown in Fig.6 together with the experimentally measured n_e-profile. This agreement with the measured profiles holds equally well also during the Ohmic phase.

3.1. Neoclassical resistive ballooning modes

For the particular conditions of shot #17529 at time t =1.29s the best fit to the experimental data Fig.4 was obtained with the neoclassical model for resistive ballooning mode driven transport, presented in Ref/7/. As ion heat transport model we used in this case χ_i =3 x χ_{CH}, which gives also a satisfactory fit to global ion parameters under these discharge conditions (although it has of course no physical basis), but poses less numerical problems than the η_i-driven transport.

The peak ion and electron temperatures predicted by this model (Fig.7a) are about 15% and the global energy confinement time 12 % below the measured ones(48 compared to 53 ms). The most positive aspect of these simulations is the good agreement of the χ_e -profile (Fig.7b) in the discharge region beyond r = 0.25 m. (In the inner regions, χ_e is strongly affected by our sawtooth model, which, by reducing the shear, enhances also strongly the resistive ballooning contribution in the region near q = 1, where a substantial pressure gradient still exists.)

Taken alone, however, the resistive ballooning model has a too weak electron temperature

dependence ($\chi_e \sim n^2 T^{1/2}$) and yields too low confinement times in purely Ohmic discharges and too high ones for stronger additional heating (see following chapter 4).

3.2. Standard trapped electron mode model.

For this model we used the formulation due to Dominguez and Waltz, given in /15/ for χ_e. It includes also a contribution of η_i-modes to the electron heat transport which is suppressed below a critical value proposed by Romanelli (see appendix A). Calculations were performed with all our four alternative ion transport models. Results for the three η_i-based model differed little, with $T_i(0)$ varying from 0.73(/4/) to 0.8kev (/15/) to 0.86 keV (/13/), reflecting an inverse variation of χ_i from 2.9 to 1.9 to 1.5 m^2/s, taken at r = 2r/3a with the radial profile of χ_i flatter in the former two cases than in the last . The corresponding variation of $T_e(0)$ was less than 0.06 keV. This illuminates the fact that a distinction between these different η_i-models will hardly be possible on the basis of ASDEX experimental data. We show here our simulation results therefore only for the two cases $\chi_i = 3 \times \chi_{CH}$ (Fig. 8a,b) and for the combined η_i model of Ref /15/ (Fig.9a,b).

The profiles of electron heat diffusivities differ little between the two cases (Figs.8b and 9b), giving values in the region 0.1 < r < 0.3 m too large by a factor 2 -3 and showing - as recognized already by many other authors - the wrong radial dependence. The electron temperatures correspondingly lie significantly below the measured values for both cases ($T_e(0)$=1.04 (Fig.8a) and 0.98 (Fig.9a) compared to 1.5 keV measured). The difference in electron temperature between the two models is significantly smaller than that of the ions ($T_i(0)$ = 0.94 (Fig.8a) and 0.80 (Fig.9a) compared to 1.35 kev measured), due to the relatively weak coupling between the two plasma components in this case.

3.3. Rogister's trapped electron mode model.

The model of Rogister leads to a completely different structure of the electron heat transport. Due to the very strong dependence of heat flow on the deviations of the electron temperature gradient from the critical one, the former remains frozen close to the limiting value given by the expression shown in the appendix A. Within a conventional transport code this leads to strong oscillations of ∇T_e, χ_e and $q_{h,e}$, which could just be handled by the code (using all the numerical tricks described in appendix B) for the heating power of our reference case, but not above. For heating powers of the Ohmic level, even the ion transport and/or another, weak underlying electron transport (like in our case 0.2 x $\chi_{Alcator}$) suffices to keep ∇T_e below the critical value for the onset of Rogister's transport. For our reference case, the resulting T_e and T_i-profiles (under the reference assumption χ_i= 3 x χ_{CH}) are close to the measured ones (Fig.10), which, however , in view of the above discussion could be largely coincidental. (A broader based comparison will be attempted later using the analysis code TRANSP). Its major

attractiveness lies in the fact that it is the only first-principle transport model predicting a confinement improvement with isotope mass, as observed experimentally.

3.4. The Rebut-Lallia transport model

The Rebut-Lallia semi-empirical transport model is based on a functional form (containing a critical temperature gradient) suggested by a picture of self-sustained magnetic turbulence, and a fit to in terms of Connor-Taylor /19/ constrained expressions using essentially JET results. We have used it both in its form as a pure electron energy transport model (in combination with the reference assumption $\chi_i = 3 \times \chi_{CH}$) and as the combined electron and ion transport model suggested later by the authors /6/. The differences between these two models in the temperature profiles are small (Figs.11a and 12a). As described in appendix B we make for numerical convenience a modification to the expression of ref./6 / which fails if $|\nabla T_e| < |\nabla T_{e,cr}|$. As $\nabla T_{e,cr}$, as given in appendix A, does not vanish at the axis, this will inevitably happen over a central region, which in our case extends over $r < 0.25$ a. At the same time, the ergodization arguments used to justify this transport model are not valid in a near shear free region, so that the T_e-values in this zone as given in fig. 11a and 12a should be simply disregarded. For the ions, in the case of the combined model, we have switched -off the Rebut-Lallia term in this region, so that T_i-profiles remain flat and credible.

For ASDEX, the Rebut-Lallia model, with the numerical constants given in ref./6/ predicts somewhat too high confinement times for purely Ohmic and too low ones for NBI heating in the 1 MW range. Depending on the chosen ion heat transport model, the "effective" electron heat diffusivities ($\chi_e = -q_{h,e} /(\partial T_e/ \partial r)$) at the time t = 1.29s are about a factor of 1.5 to 2 larger than those determined by the TRANSP analysis code (Figs. 11b, 12b). Correspondingly, during this phase the plasma temperatures (and the gradients, except in the innermost zone) are considerably smaller in the simulation than in reality. On the other hand, during the Ohmic phase, the measured electron temperature gradients lie systematically below the critical values given by Rebut and Lallia . Within the framework of the functional form postulated by them, these results would become compatible if one would assume smaller values of the critical temperature gradient and of the anomalous diffusivity (χ_2 in formula B3 in appendix B) for ASDEX than for JET.

3.5. Becker's L-mode transport model.

We have used Becker's transport model in the form given in ref. /9 /, where separate, not continuously connected expressions for χ_e were given for the Ohmic, namely the Coppi-Mazzucato-Gruber heat diffusivity /20/, and L-mode additional heating phases of discharges. The L-mode expressions were empirically derived in simulations of ASDEX results, with the Connor-Taylor constraints used to fix the major-radius dependence of the diffusivity.

The temperatures simulated with this model are substantially too low (fig.13a). This is a consequence of χ_e exceeding the one derived from the TRANSP analysis by a factor of 3 (fig.13b). the radial dependence of χ_e has approximately the right form. This partly reflects the fact that Becker's fits refer primarily to cases with high additional heating power. In fact, in a later work he proposed a formula containing a continuous transition from Ohmic to L-regime transport (and hence reduced values of χ_e in the intermediate power regime), which however has not been used so far in any actual simulations. A second reason for these differences is that in the above simulations we have used (for consistency in the comparison with the other transport models and to take into account results of our TRANSP analyses) $\chi_i = 3 \times \chi_{CH}$, whereas Becker's fits assumed $\chi_i = \chi_{CH}$.

4. Simulation of Power Scans

As a much larger data base exists for global confinement times than for local power balances, we have carried out a power scan with all the transport models described above. As fixed parameters we have kept a line-average density of $\overline{n}_e = 4.5 \times 10^{19} m^{-3}$, $B_t = 2.3$ T and a plasma current of 440 kA. The heating power was varied in the calculations over a range exceeding even our experimental possibilities. (In particular however we are usually not capable to avoid an H-mode transition for $P_{NBI} > 1.6$ MW at these densities, so that the highest power experimental point used in the present comparison were taken from the transient L-phase of an H-mode discharge.) To be consistent with the measured radiated power fractions we have adjusted the impurity inflow so as to keep a constant $P_{rad}/P_{tot} \approx 0.3$. Using the Coronal model this implied a steady increase of the impurity content with power leading to a variation of Z_{eff} from 1.2 (Ohmic) to 2.5 at the highest heating powers ($P_{tot} \approx 4.6MW$).

For two electron heat transport models (trapped electron modes and Rebut-Lallia) we have carried out simulations with alternative ion transport expressions. For the case of the strong electrostatic turbulence models (trapped electron and η_i-modes) little difference among the three different formulations of η_i-mode transport had already been found in the radial power balance (see section 3.2) and this was found to be even more so for the global energy confinement behaviour. Fig. 14 shows that for τ_E even the difference between these self-consistent χ_i-models and our ad-hoc reference model $\chi_i = 3 \times \chi_{CH}$ is small. Fig. 15 shows that the same holds also for the two ion transport versions used in connection with the Rebut-Lallia electron transport model. In the following discussion of the power dependence of the energy confinement time (Fig.16) we will therefore consider only the combinations with the reference χ_i- model.

The neoclassical resistive ballooning model, which gave the best fit to the low-power NBI case of chapter 3, shows, due to the $\chi_e \sim n^2 T^{1/2}$ variation, a too weak power dependence in such a constant density scan.

The trapped electron mode model, on the other hand, yields approximately the right power dependence, but approximately 30% too low values for τ_E. These corresponding differences between theory and experiment in the local χ_e-values are even much larger than that. In the simulation calculations, where the enhanced electron transport results in a reduced T_e-values, the theoretical χ_e-values are approximately a factor of 2 larger than those deduced by energy balance analysis with the TRANSP code (Fig. 4). Evaluating the theoretical χ_e-expressions using the *measured* T_e-profiles yields discrepancies reaching even up to an order of magnitude, reflecting the strong nonlinearity of $\chi_e(T_e)$.

The dissipative trapped electron mode should give rise to (for given B_t, r, q, and temperature and density decay lengths) $\chi_e \sim T^{7/2}/n_e$, the collisionless trapped electron modes $\chi_e \sim T^{3/2}$. If χ_e were exclusively responsible for energy confinement, this would give rise to $\tau_E \sim n\, P_{tot}^{-7/9}$ in the former and $\tau_E \sim n^{3/5}\, P_{tot}^{-3/5}$ in the latter regime. A logarithmic plot (Fig.17) of the simulated $\tau_E\,(P_{tot})$ reveals indeed a change in exponent with heating power (and thus collisionality). Particularly in the collisionfree, high-power regime, however, the power dependence found in the simulations is, however, weaker than predicted by the above expressions. This is to one part due to the contribution of the slowing down NB-injected particles to the total plasma energy (see /21/), which is fully included in the definition used here. To verify this statement, we also show the confinement time of the purely thermal plasma, showing a closer approach to the above scaling. (In Fig.17 we have used the results of the full electro- static strong turbulence model, as $\chi_{\eta i}$, which dominates the ion transport, has the same temperature and density dependence as the collisionless trapped electron modes). This example illustrates the danger inherent in relating in a simple way global confinement to local transport coefficients.

The model by Rebut-Lallia gives, as already mentioned in section 3.4, somewhat too good confinement in the Ohmic regime and a too steep power degradation at intermediate heating powers indicating, at least, that the expressions for $\nabla T_{e,\,cr}$ and χ_2 given in appendix A, are not universally valid for all devices. The results would become compatible if one would assume smaller values of both quantities for ASDEX than for JET.

The expression given by Becker used in our simulations contains no implicit temperature and density dependence, and cannot, in this form, describe the gradual confinement variation at small and intermediate additional heating powers. The discrepancy between these simulations and the experimental results even at high heating powers is presumably due to the different ion heat transport models used in our simulations ($\chi_i = 3 \times \chi_{CH}$) and by Becker in the fitting.

5. Conclusions

The transport model having the best developed first principle basis is the one based on strong electrostatic turbulence. One element of it, the contribution of the η_i-driven modes to the ion heat conductivity has been very successful in explaining the observed response of confinement to density profile changes on ASDEX in the IOC, pellet refuelled and ctr-NBI discharges (refs. /18, 22/). It has been found to be even in good *quantitative* agreement with measurements over a range of confinement regimes (LOC, SOC, L- and H-mode discharges), and it explains the improvements of toroidal angular momentum confinement in the transitions from co- to ctr- NBI-injection which lead to a peaking of the density profiles / 23/.

Regarding the electron branches, our analysis and simulations show that trapped electron driven turbulence predicts at least the correct power dependence of confinement time. The χ_e-values postulated by it in the interior plasma regions (at least outside the sawtooth-region) are too large by typically half an order of magnitude, which is certainly within a reasonable claim of accuracy of such theories. These modes can, however, not explain the observed radial increase of χ_e towards the boundary.

Resistive ballooning modes, in their "neoclassical" form proposed by Callen et al./7/, on the other hand, show the correct radial dependence of χ_e, but have (in a constant density scan) a too weak power dependence ($\tau_E \sim n^{-1}P^{-1/3}$). This suggests, as a promising model, a combination of it with the strong electrostatic turbulence transport. The latter would dominate in the interior plasma zones and enhance the power degradation, whereas the resistive ballooning modes would explain the radial increase of χ_e in the outer layers. The detailed weighting of the two transport channels might vary from experiments to experiment (and plausibly also with heating method) explaining the variation of the quoted power dependencies of τ_E. The opposing density dependencies of the two transport mechanisms, on the other hand, might ultimately explain the observed small variation of global confinement time with density.

Based on our investigations we can at present, however, not exclude that magnetic rather than electrostatic turbulence could be dominating also in the interior zones, in a form suggested, e.g. by the self-sustained magnetic turbulence model of Rebut and Lallia.

The major criticisms also against this model concerns the expected isotope dependence of confinement, as all its contributions predict an increase or at best invariance of transport with increasing ion mass, in contrast with our experimental observations.

References

/1/   R.J. Goldston et al.,J.Comp.Phys., **43** (1981) 61

/2/   D.E. Post, C.E. Singer, A.M. McKenney, Baldur: Rep. 33, PPPL, Princeton (1981)

/3/   F. Romanelli, W.M. Tang, R.B. White, Nucl.Fusion **26** (1986) 1515

/4/   R. Dominguez, R.E. Waltz, Nucl. Fusion **27** (1987) 65

/5/   P.H. Rebut, M. Brusati, Plasma Phys. and Contr. Fusion **28** (1986) 113

/6/   P.P. Lallia, P.H. Rebut, M.L. Watkins, JET Report JET-P(88)05

/7/   J.D. Callen, W.X. Qu, K.D. Siebert, et al., Plasma Phys. and Contr. Fus. Res., IAEA, Vienna, II (1987) 157

/8/   B.A. Carreras et al., Phys. Rev. Lett., **50** (1983) 503

/9/   G. Becker, Nucl. Fusion **28** (1988) 1458

/10/   A. Rogister, Nucl. Fusion **28** (1988) 1053

/11/   C.S. Chang, F.L. Hinton, Phys. Fluids **25** (1982) 1493

/12/   C.S. Chang, F.L. Hinton, Phys. Fluids **29** (1986) 3314

/13/   N. Mattor, P.H. Diamond, Phys. Fluids **31** (1988) 1180

/14/   W. Horton, D-I. Choi, W.M. Tang, Phys.Fluids **24** (1981) 1077

/15/   R.W. Ross, P.H. Diamond, J.F. Drake, et al., Report DOE/ET-53913-7 and University of Texas Fusion Research Center Report #295 (1987)

/16/   F. Romanelli, S. Briguglio, JET Report JET-P(88)

/17/   W.M. Tang, Nucl.Fusion **26** (1986) 1605

/18/   O. Gruber, H.U. Fahrbach, O. Gehre, et al., Plasma Phys. and Contr. Fusion **30** (1988)1611

/19/   J.W. Connor, J.B. Taylor, Nucl. Fusion **17** (1984) 87

/20/   O. Gruber, Nucl. Fusion **22** (1982) 1349

/21/   K. Lackner, O. Gruber, R. Wunderlich, IPP Report IPP 5/28 (1989)

/22/   K. Lackner, O. Gruber, F. Wagner, et al., Confinement Regime Transitions in ASDEX, Plasma Physics and Controlled Fusion (1989), to be published

/23/   O. Gruber, A. Kallenbach, H.-U. Fahrbach, et al., Proc. 16th Europ. Conf. on Contr. Fus. and Plasma Physics, **13B** (1989) Part I, 171

Appendix A

Anomalous electron and ion heat diffusivities

1. Electron transport by resistive ballooning modes

1. author: B.A. Carreras et al., /8/

$$\chi_{e,1} = \frac{3}{2\mu_0\sqrt{2}q} * \frac{v_{th,e}}{v_A} * \eta * \left(\beta_p\varepsilon^2\frac{L_s}{L_p}\right)^{3/2}$$

with

$$\eta = \frac{m_e}{e^2} * \frac{(2.67 + Z_{eff})}{3.4(1.13 + Z_{eff})} * \frac{\nu_{ei}}{n_e}$$

$$L_s = \frac{RqL_q}{r} \qquad L_q = \frac{q}{\left|\frac{\partial q}{\partial r}\right|} \qquad L_p = \frac{k(n_eT_e + n_iT_i)}{\left|\frac{\partial k(n_eT_e + n_iT_i)}{\partial r}\right|}$$

$$v_a = \frac{B_t}{\sqrt{\mu_0 n_e m_p A_i}}, \qquad v_{th,e} = \left(\frac{2kT_e}{m_e}\right)^{1/2}, \qquad \beta_p = \frac{2\mu_0 k(n_e T_e + n_i T_i)}{B_p^2}$$

2. author: J.D. Callen et al., /7/

$$\chi_{e,2} = \chi_{e,1} * \frac{7.05}{\varepsilon^{3/2}} \qquad \text{with} \qquad \varepsilon = \frac{r}{R}$$

2. Electron transport by trapped electron modes
author: R. Dominguez, R.E. Waltz /4,15/

$$\chi_e = \varepsilon^{3/2} * \left(\frac{\rho_s c_s}{L_{n_e}}\right)^2 * \frac{1}{\nu_{ei}} * \frac{5}{2}\eta_e * f, \qquad \text{if} \qquad \frac{\omega_e^*}{\omega_{b_e}} < \nu_e^* (\text{DTEM})$$

$$\chi_e = 3\varepsilon^{1/2} * \frac{\rho_s^2 c_s}{L_{n_e}} * \frac{5}{2}\eta_e * f, \qquad \text{if} \qquad \frac{\omega_e^*}{\omega_{b_e}} > \nu_e^* (\text{CTEM})$$

with:

$$\varepsilon = \frac{r}{R}, \qquad \rho_s = \frac{c_s}{\omega_{ci}} = \frac{c_s m_p A_i}{e B_t}, \qquad \nu_{ei} = \frac{Z_{eff}}{\tau_e}$$

$$c_s = \left(\frac{kT_e}{m_p A_i}\right)^{1/2}, \qquad \omega_e^* = \frac{c_s}{3 L_{n_e}}, \qquad \omega_{b_e} = \frac{\varepsilon^{1/2} v_e}{qR}$$

$$v_e = \left(\frac{2kT_e}{m_e}\right)^{1/2}, \qquad \nu_e^* = \nu_{ei} * \frac{qR}{v_e \varepsilon^{3/2}}, \qquad \eta_e = \frac{L_{n_e}}{L_{T_e}} = \frac{n_e}{\left|\frac{\partial n_e}{\partial r}\right|} * \frac{\left|\frac{\partial T_e}{\partial r}\right|}{T_e}$$

$$\nu_{ei} = \frac{4\sqrt{2}\pi e^4 n_e \ln \Lambda_e Z_{eff}}{3(4\pi\varepsilon_0)^2 \sqrt{m_e}(kT_e)^{3/2}}$$

$$f = 1 + 3\theta * \frac{L_{n_e}}{L_{T_e}} * \frac{L_{n_e}}{R} = 1 + 3\theta * \eta_e * \frac{L_{n_e}}{R}$$

$$\theta = \frac{1}{2} + \frac{3(\eta_e - \eta_{e,th})}{4\Delta\eta_e} - \frac{(\eta_e - \eta_{e,th})^3}{4\Delta\eta_e^3}$$

Taking $\eta_e^* = \frac{\eta_e - \eta_{e,th}}{\Delta\eta_e}$, i.e. $\eta_e = \eta_e^* \Delta\eta_e + \eta_{e,th}$, we obtain

$$\theta = \frac{1}{2} + \frac{3}{4}\eta_e^* - \frac{1}{4}\eta_e^{*3} = \frac{1}{4} * (\eta_e^* + 1)^2 * (2 - \eta_e^*).$$

Asymptotic behaviour for the function θ :

$$\theta = 0 \quad \text{for} \quad \eta_e \leq \eta_{e,th} - \Delta\eta_e \Rightarrow \eta_e^* \leq -1$$
$$\theta = 1 \quad \text{for} \quad \eta_e \geq \eta_{e,th} + \Delta\eta_e \Rightarrow \eta_e^* \geq 1$$

3. Ion transport by η_i - modes

$$\chi_i = F * G * \frac{\rho_s^2 c_s}{0.3 L_{n_i}} \sim \frac{T_e^{3/2} A_i^{1/2}}{B_t^2}.$$

$$L_{n_i} = \frac{n_i}{\left|\frac{\partial n_i}{\partial r}\right|}, \qquad L_{T_i} = \frac{T_i}{\left|\frac{\partial T_i}{\partial r}\right|}, \qquad L_q = \frac{q}{\left|\frac{\partial q}{\partial r}\right|}, \qquad L_s = \frac{R q L_q}{r},$$

$$\eta_i = \frac{L_{n_i}}{L_{T_i}}, \qquad c_s = \left(\frac{k T_e}{m_p A_i}\right)^{1/2}, \qquad \rho_s = \frac{c_s}{\omega_{ci}} = c_s * \frac{m_p A_i}{e B_t}.$$

1. author: R.W. Ross et al. /13,14,15/

$$F * G = \theta(\eta_1^*) * \theta(\eta_2^*) * \frac{\sqrt{1+\eta_i}}{3} * \frac{L_s}{R} + \theta(\eta_3^*) * 0.39 * \frac{L_{n_i}}{L_s} * \left(\frac{\pi}{3}(1+\eta_i)\ln(1+\eta_i)\frac{T_i}{T_e}\right)^2$$

2. author: R. Dominguez, R.E. Waltz /4,15/

$$F * G = \theta(\eta_1^*) * \frac{5}{2}\left(\frac{2 T_i}{T_e}\eta_i\frac{L_{n_i}}{R}\right)^{1/2}$$

3. author: N. Mattor, P.H. Diamond /13/

$$F * G = \theta(\eta_1^*) * 0.39 * \frac{L_{n_i}}{L_s} * \left((1+\eta_i)\frac{T_i}{T_e}\right)^2$$

with

$$\theta(\eta_k^*) = \frac{1}{2} + \frac{3}{4}\eta_k^* - \frac{1}{4}\eta_k^{*3} = \frac{1}{4} * (\eta_k^* + 1)^2 * (2 - \eta_k^*);$$

$$\eta_1^* = \frac{\eta_i - \eta_{i,th}}{\Delta\eta_i}; \qquad \eta_2^* = \frac{2\eta_{i,th} - \eta_i}{\Delta\eta_i}; \qquad \eta_3^* = \frac{\eta_i - 2\eta_{i,th}}{\Delta\eta_i};$$

To have the true asymptotic behaviour of θ we set

$$\eta_k^* = \max(\eta_k^*, -1) \quad \text{and} \quad \eta_k^* = \min(\eta_k^*, 1).$$

Influence of long density decay lengths is included according to F. Romanelli /16/

$$\eta_{i,th} = \max\left(\eta_{i,th}, \eta_{i,th} + \eta_{imu} * (1 + \frac{T_i}{T_e}) * (\frac{L_{n_i}}{R} - \eta_{imo})\right)$$

Values assumed: $\eta_{i,th} = 1.5; \quad \Delta\eta_i = 0.4; \quad \eta_{imu} = 1.0; \quad \eta_{imo} = 0.2.$

4. Electron transport by trapped electron modes
author: A. Rogister /10/

Definition of γ^* :

$$\gamma^* = 2,3 * 10^{20} * \mu * \frac{\varepsilon^{3/2} T_e^2 L_s b_n(\sqrt{\nu_{e,R}^*})}{\sqrt{A_i} L_{n_e} L_{T_e} n_e (1 + Z_{eff})}$$

with

$$\varepsilon = \frac{r}{R}, \qquad L_s = \frac{Rq^2}{r|\frac{\partial q}{\partial r}|}, \qquad L_{n_e} = \frac{n_e}{|\frac{\partial n_e}{\partial r}|}, \qquad L_{T_e} = \frac{T_e}{|\frac{\partial T_e}{\partial r}|}$$

$$b_n(t) = \left(1 + t + \frac{t^2}{2} + \frac{t^3}{3}\right) * e^{-t}, \qquad \nu_{e,R}^* = \sqrt{2} * \nu_e^* * \left(1 + \frac{1}{Z_{eff}}\right)$$

$$\nu_e^* = \nu_{ei} * \frac{qR}{v_e \varepsilon^{3/2}}, \qquad \nu_{ei} = \frac{4\sqrt{2\pi} e^4 n_e \ln \Lambda_e Z_{eff}}{3(4\pi\varepsilon_0)^2 \sqrt{m_e}(kT_e)^{3/2}}$$

If $\gamma^* \leq 1$: $\qquad\qquad \chi_e = 0$

If $\gamma^* > 1$:

$$\chi_e = 4.25 * 10^{22} * \frac{\varepsilon^{3/2} T_e^{7/2}(1 + \frac{0.4}{\eta_e})}{qRL_s B_t^2 n_e(1 + Z_{eff})} * b_p(\sqrt{\nu_{e,R}^*}) * \bar{g}(x) * (\gamma^* - 1)^{4.63} * \frac{\nu_{eff}^2}{\nu_{eff}^2 + \omega_{e,R}^{*2}}$$

with

$$\eta_e = \frac{L_{n_e}}{L_{T_e}}, \qquad \nu_{eff} = \frac{\nu_{ei}}{\varepsilon} * \left(1 + \frac{1}{Z_{eff}}\right), \qquad \omega_{e,R}^* = \frac{0.62 c_s}{(1 + 0.62^2) L_{n_e}},$$

$$b_p(t) = \left(1 + t + \frac{t^2}{2} + \frac{t^3}{6} + \frac{t^4}{15}\right) * e^{-t}$$

$$\bar{g}(x) = (1 - e^{-7.87x}) * \frac{1 + 1.54x}{1 + 3.685x + 0.0707x^2}, \qquad x = \frac{L_{n_e} L_s}{q^2 R^2} - 0.004 .$$

5. Critical temperature gradient model
author: P.H. Rebut, P.P. Lallia, Varenna-meeting (1987) and /6/

Definition of a critical temperature gradient

$$\nabla T_{e,cr} = 5.0 * \left(\frac{U_1 B_t^3 10^{19}}{n_e \sqrt{T_e} 2\pi R} \right)^{1/2} * \frac{1}{q}$$

If $\nabla |T_e| < \nabla T_{e,cr}$: $\chi_{e,i}$ (anomalous) $= 0$

If $\nabla |T_e| > \nabla T_{e,cr}$: $\chi_e = \chi_2 * \dfrac{|\frac{\partial T_e}{\partial r}| - \nabla T_{e,cr}}{|\frac{\partial T_e}{\partial r}|}$

$$\chi_i = \chi_e * Z_i (T_e/T_i)^{1/2}$$

with $\chi_2 = 0.6 * \left(\dfrac{1}{L_{T_e}} + 2\dfrac{1}{L_{n_e}} \right) * \left(\dfrac{T_e}{T_i} \right)^{\frac{1}{2}} * \dfrac{R}{r} * \dfrac{1}{\frac{|\partial q/\partial r|}{q^2} * B_t \sqrt{R}}$

and $L_{T_e} = \dfrac{T_e}{|\frac{\partial T_e}{\partial r}|}$ $L_{n_e} = \dfrac{n_e}{|\frac{\partial n_e}{\partial r}|}$

6. Electron transport (empirical)
author: G. Becker /9/

$$L - \text{mode} : \chi_e = 6.2 * \frac{q}{B_t \sqrt{RA_i}}$$

$$H - \text{mode} : \chi_e = 2.5 * \frac{q}{B_t \sqrt{RA_i}}$$

$$H^* - \text{mode} : \chi_e = 1.3 * \frac{q}{B_t \sqrt{RA_i}}$$

The formula are applied inside $r \leq r_{sep} - 3cm$, whereas in the region $r_{sep} - 3cm < r < r_{sep}$ χ_e is extrapolated to zero.

Appendix B: Numerical Treatment of the Transport Terms

For the energy transport models discussed in the introduction, the conductive heat flux of the k-th species

$$q_{h,k} = - n_k \chi_k \frac{\partial}{\partial r} T_k \qquad \text{... (B1)}$$

includes contributions to χ_k of the form

$$\chi = \chi_0 \left| \frac{\partial T}{\partial r} \right|^\alpha + \chi_1 + \chi_2 \cdot \max\left(\sigma, 1 - \frac{(\partial T/\partial r)}{(\partial T/\partial r)_\alpha} \right) + \chi_3 T^\gamma \qquad \text{... (B2)}$$

where the χ_i can still depend on r and plasma parameters other than T_k.

We have studied in stand -alone calculations three different solution procedures for time dependent energy balance equations under transport laws of the above form:

(i)   implicit in T, but computing χ from the T-values at the old time step

(ii)   like above, but including an additional predictor-corrector step for the calculation of χ, using in the corrector step the time-centered value of χ

(iii)   a Taylor expansion of χ with respect to T and $\partial T/\partial r$ and an inclusion of all terms linear in the new time step value of T in the implicit formulation.

In our actual transport simulation calculations we have used however only the method (ii), which is compatible with the standard BALDUR coding.

In addition, for the η_i-mode and the Rogister-TEM models, which contain hard switch-on criteria for the transport enhancements, we used spatial averaging of the gradients over 3 or 5 radial grid-points to reduce oscillations.

The problems with a hard onset of a transport channel exists also in the Rebut-Lallia model, where the relation between q and $\partial T/\partial r$ is

$$q_{h,k} = - n_k \chi_1 \frac{\partial}{\partial r} T_k - n_k \chi_2 \left(\left(\frac{\partial T_k}{\partial r} \right) - \left(\frac{\partial T_k}{\partial r} \right)_\alpha \right) \cdot H \left(\left(\frac{\partial T_k}{\partial r} \right)_\alpha - \left(\frac{\partial T_k}{\partial r} \right) \right) \qquad \text{... (B3)}$$

in terms of the Heaviside function H, with χ_1 an underlying transport active also when the "Rebut-Lallia" term $\sim \chi_2$ is suppressed. As the authors of this model content that the condition $|\partial T/\partial r| > |\partial T/\partial r|_{cr}$ is nearly always satisfied, we have substituted equ. B3 by the expression

$$q_{h,k} = - n_k (\chi_1 + \chi_2) \frac{\partial}{\partial r} T_k + n_k \chi_2 \left(\frac{\partial T_k}{\partial r} \right)_\alpha \qquad \text{... (B4)}$$

which is identical to it for $|\partial T/\partial r| > |\partial T/\partial r|_{cr}$ and corresponds to the substitution of the solid by the dashed line in Fig.B1 below for $|\partial T/\partial r| < |\partial T/\partial r|_{cr}$. Expression B4 obviously poses no problem in the numerical treatment (it corresponds to a pinch term like generally used in the particle transport equation). Results obtained with it have however to be checked a posteriori to see whether the validity condition of the approximation was justified. For the "background transport" term we used χ_1 equal to $0.2 \cdot \chi_{Alcator-Intor}$.
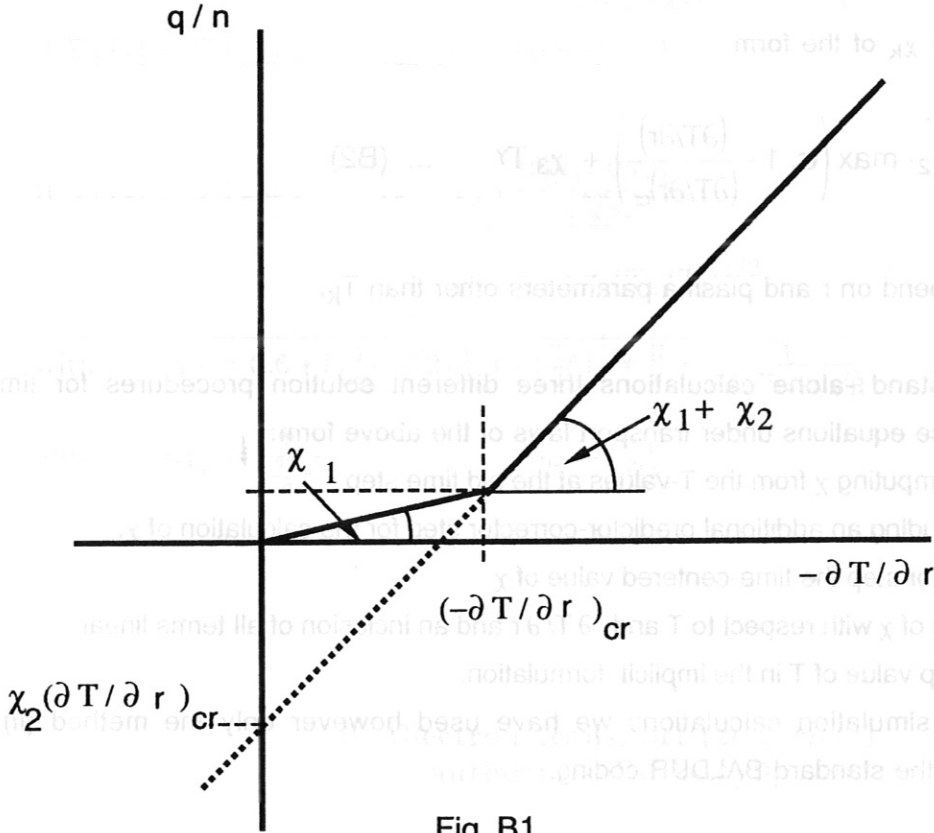
Fig. B1

Fig.B1: Relation between heat flux q and temperature gradient according
to the model of Rebut-Lallia (solid line) and as actually used in
our simulations (dotted line)
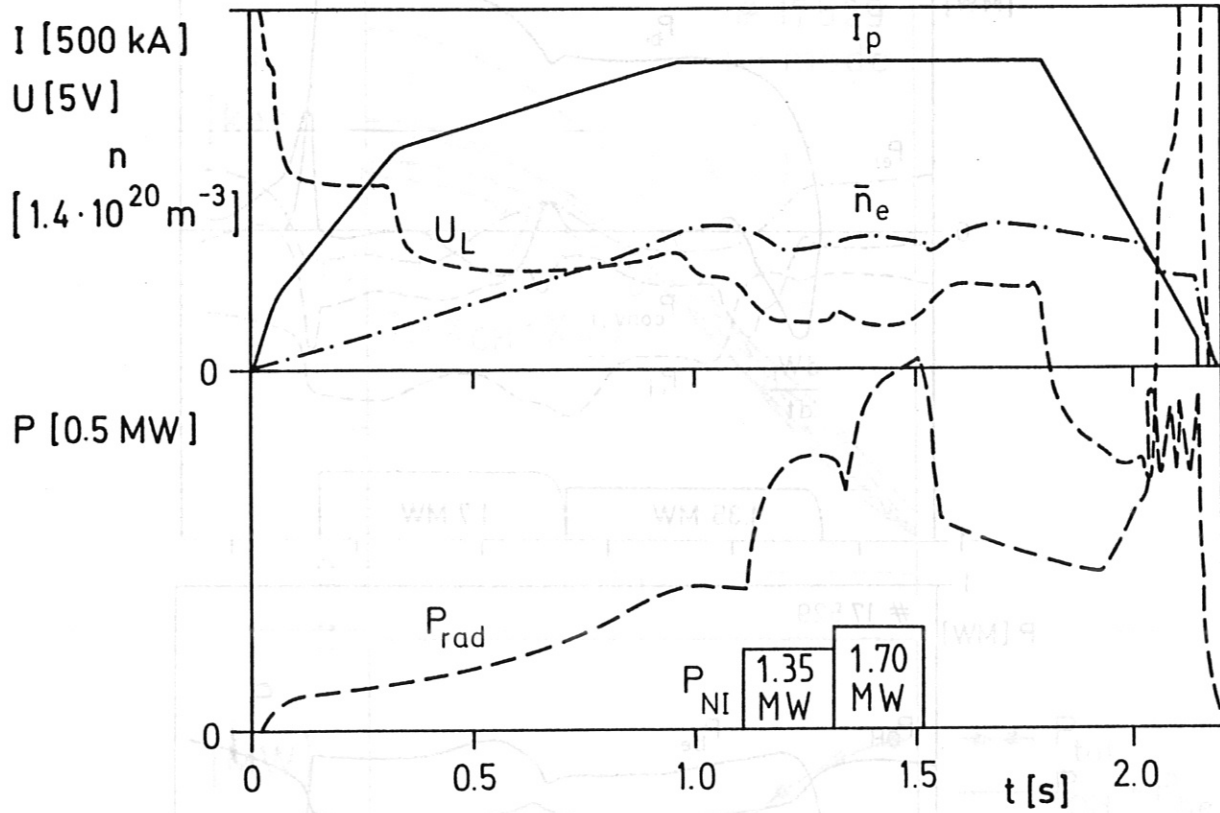
Fig.1 Time-traces of plasma current (I_p), loop-voltage (U_L), line averaged electron
density through a mid-plane chord ($\bar{n}_e$), total radiated power(P_{rad}) and beam power
P_{NI} of the discharge #17529.
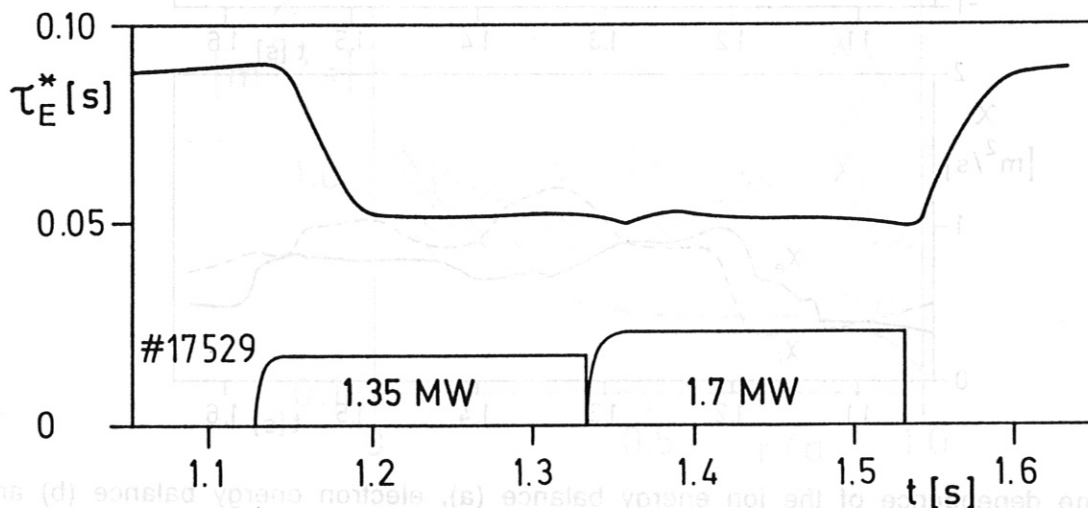
Fig.2 Energy replacement time τ_E^* (from diamagnetic signal) vs. time.
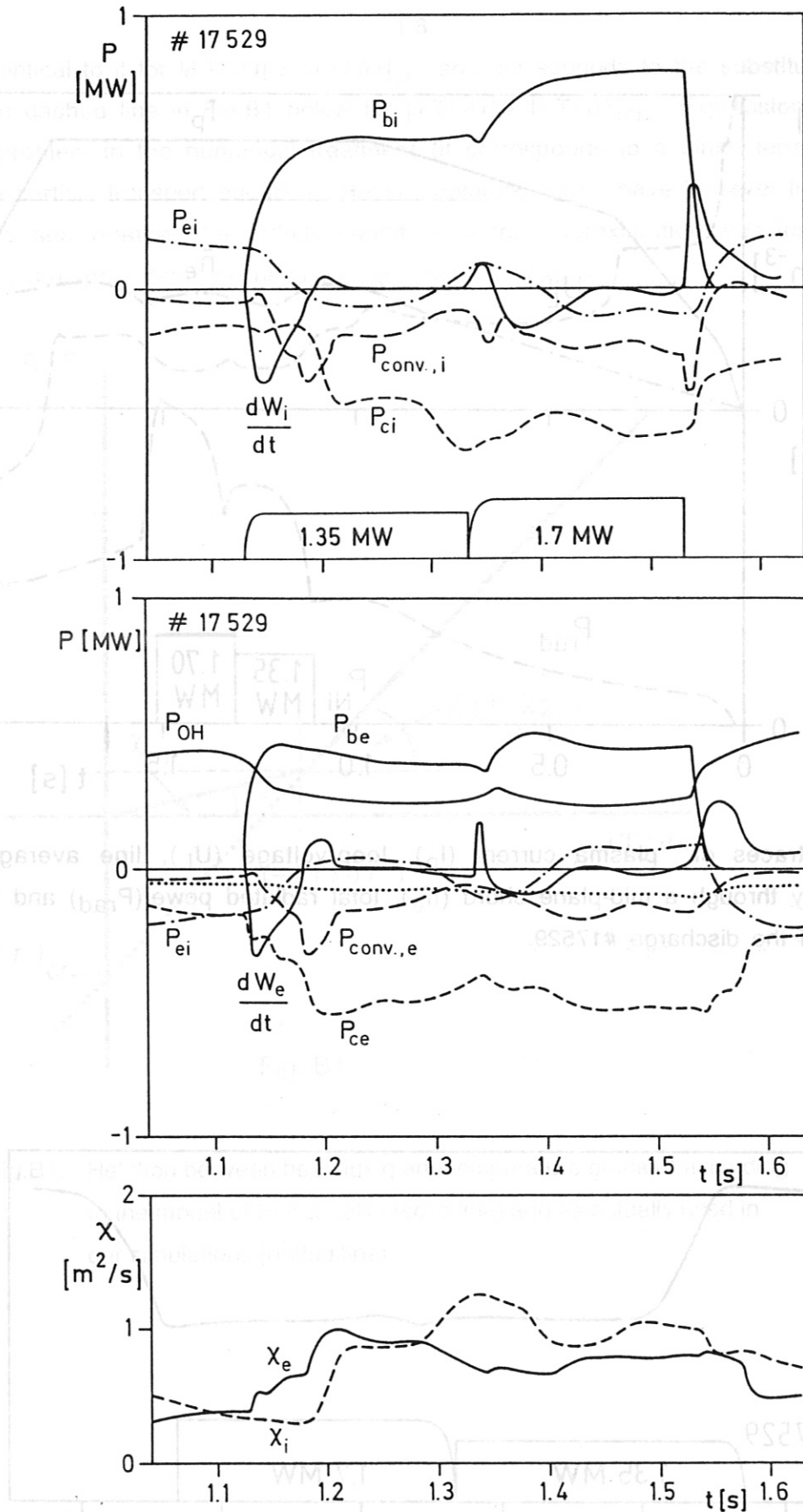
Fig.3 Time dependence of the ion energy balance (a), electron energy balance (b) and "effective" ion and electron heat diffusivities $\chi_{i,e}$ (c) at $r=2/3a$ from TRANSP analysis (W kinetic energy, P_C heat conduction power, P_{conv} convection power, P_b beam heating power, P_{OH} Ohmic heating power)
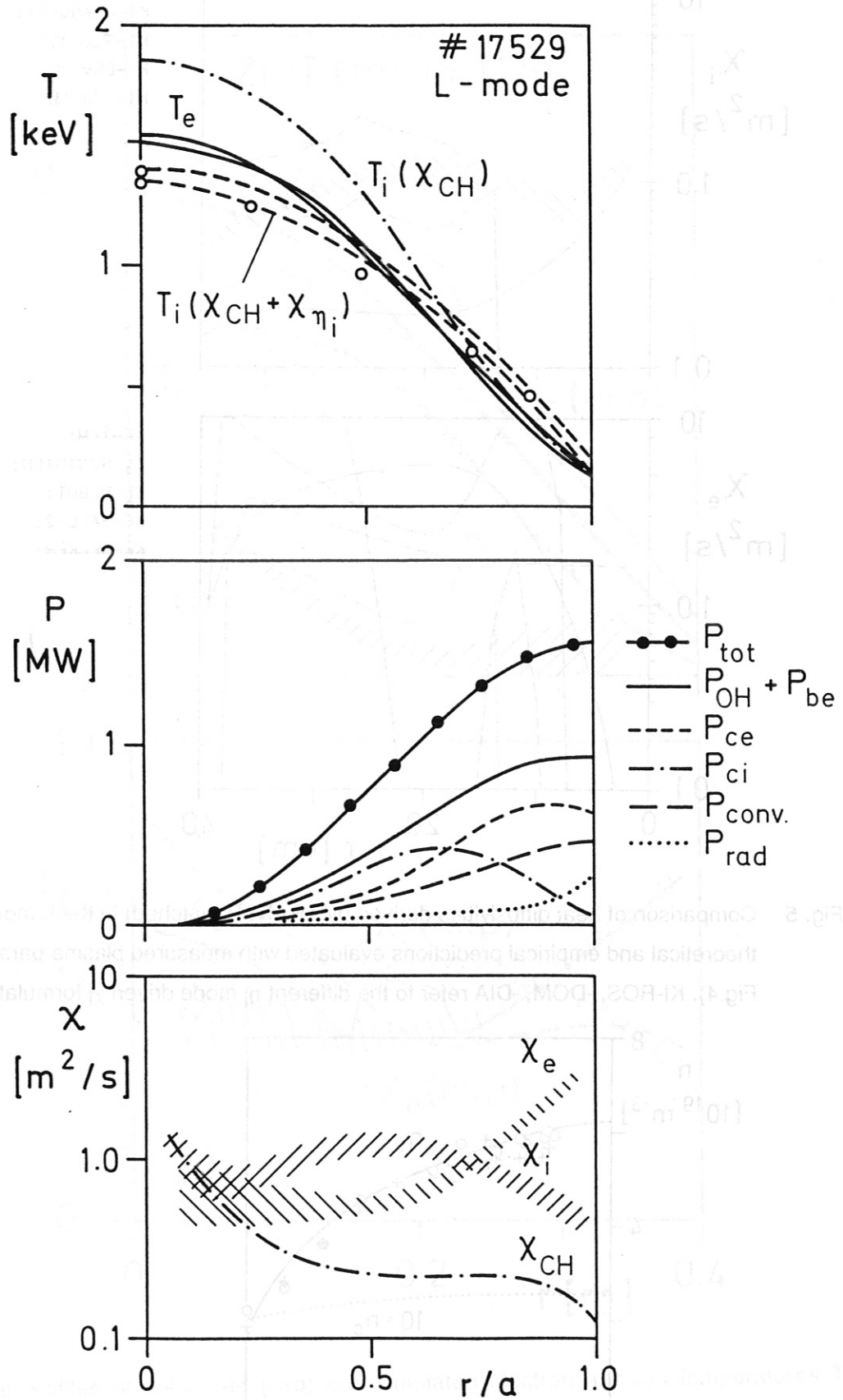
Fig.4 Profiles of temperatures, heating power and loss power fluxes and heat diffusivities in L-regime co-NBI heated discharge phase. T_i is obtained by TRANSP analysis with $\chi_i = \chi_{CH} + \chi_{\eta i}$ and χ_{NC}, resp., and has to be compared with the passive CX measurements (o).

KI−CHANG−HI :	LINEAR
KI−ROS /15/ :	DASHED
KI−DOM/15/ :	DOT−DASHED
KI−DIA/13/ :	DOTTED

KE−TEM:	LINEAR
KE−ROGISTER:	DASHED
KE−REBUT:	DOT−DASHED
KE−BALL−2:	DOTTED
KE−BECKER:	DOT−DASHED
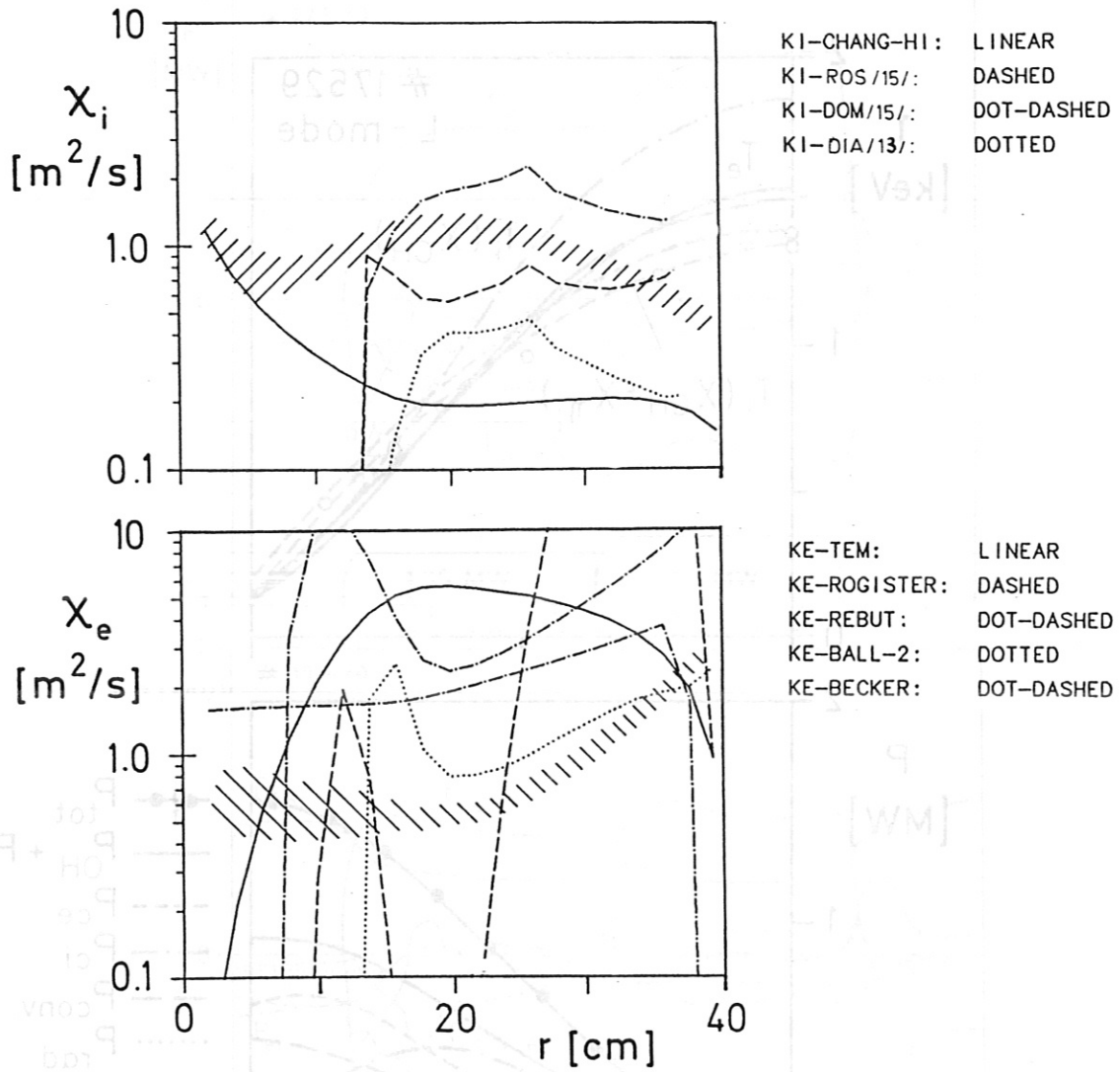
Fig. 5   Comparison of heat diffusivities derived by TRANSP (hatched) in the L-mode phase with theoretical and empirical predictions evaluated with measured plasma parameters (see Fig.4). KI-ROS, -DOM, -DIA refer to the different η_i mode driven χ_i formulations used.
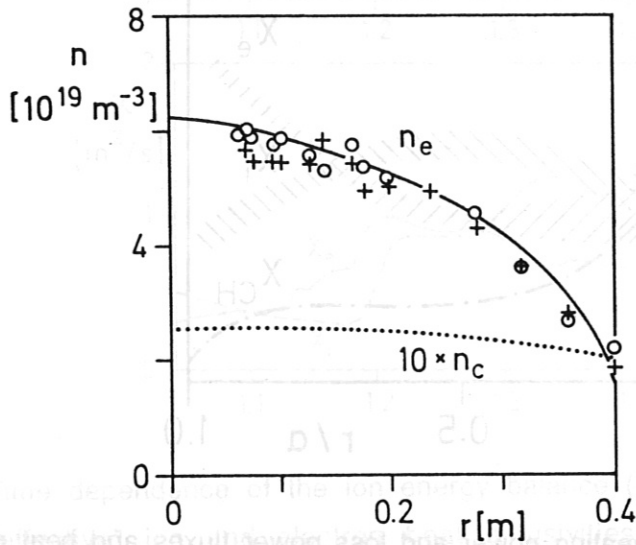
Fig.6   Calculated profiles of electron and impurity densities at the reference time 1.29 sec of the L-mde discharge phase together with the experimentally measured n_e values.
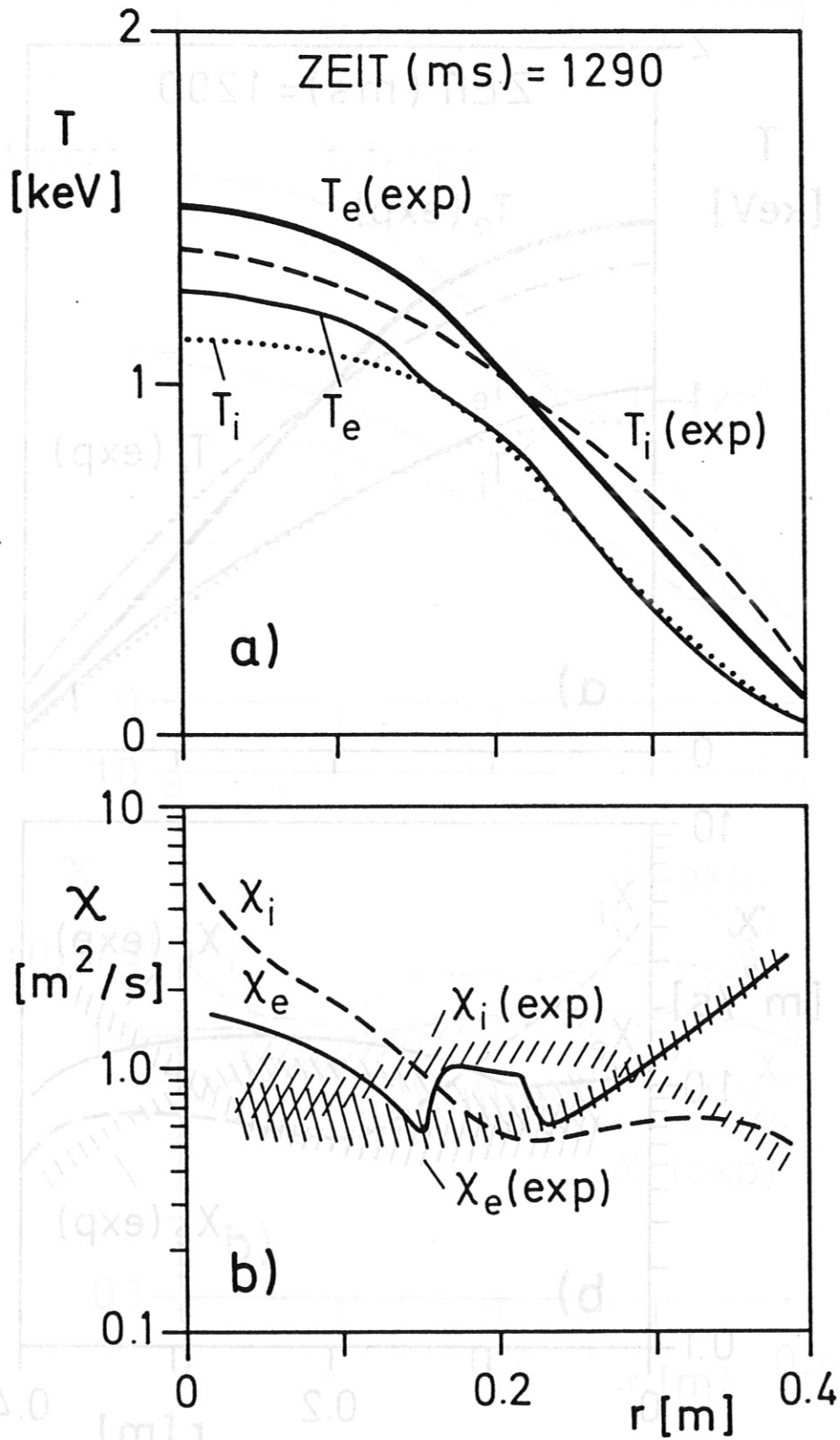
Fig.7 Radial profiles of measured (exp) and simulated electron and ion temperatures $T_{e,i}$ in the L-mode phase using χ_e from neoclassical resistive ballooning mode theory (Appendix A-1/7/) and $\chi_i = 3 \times \chi_{CH}$ (a). These electron and ion heat diffusivities $\chi_{i,e}$, resp., are compared with the measured ones (exp) in (b).
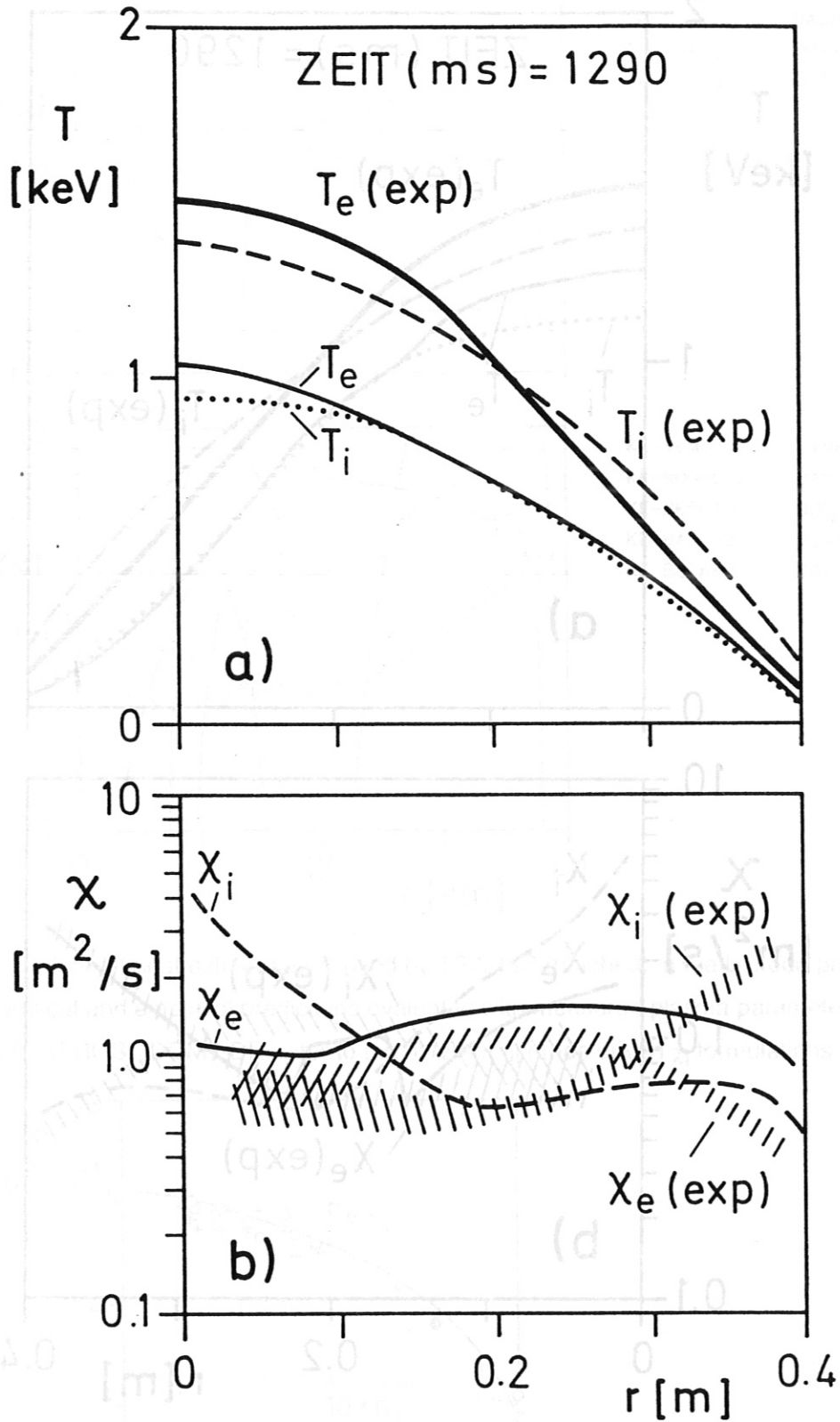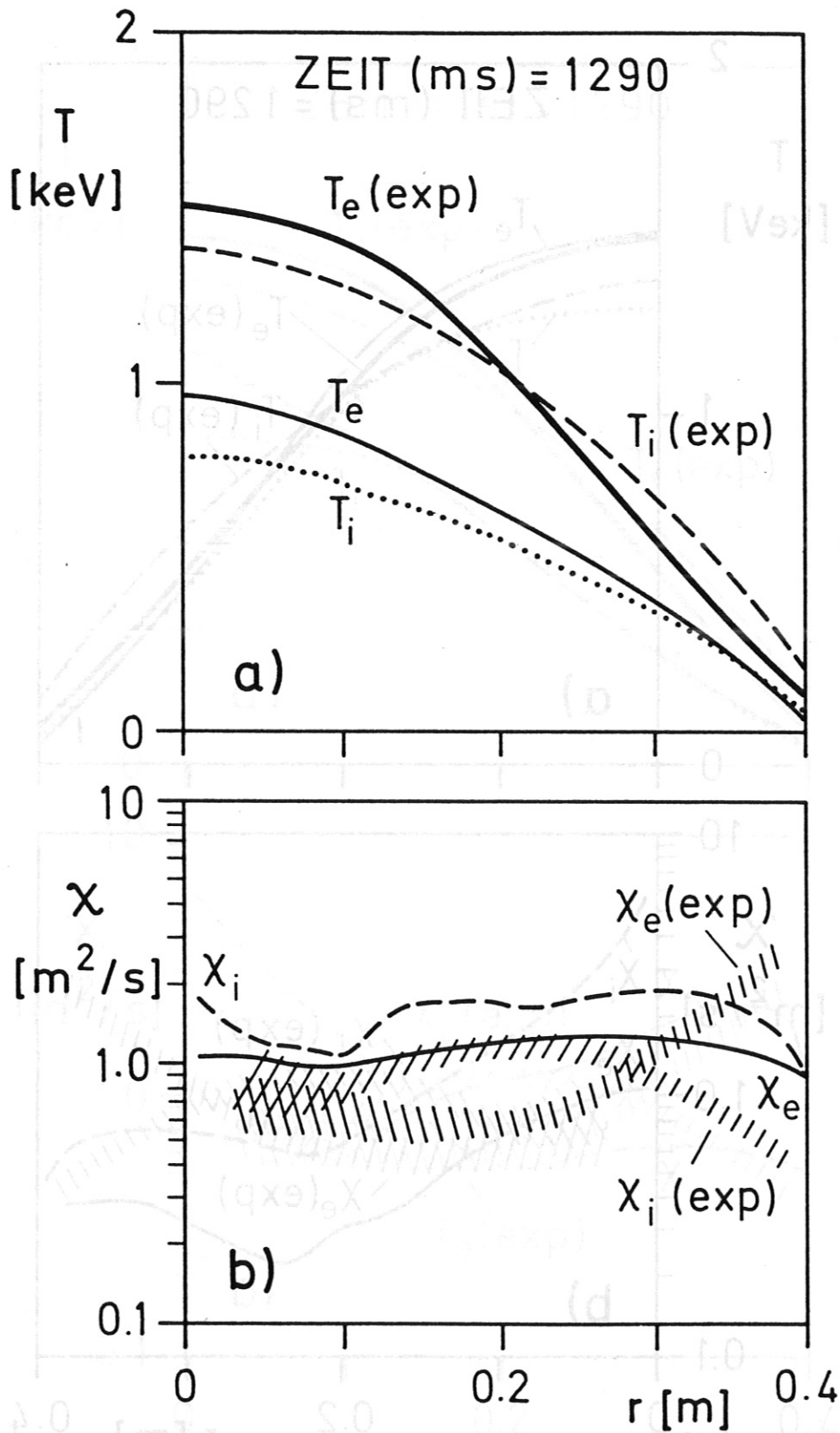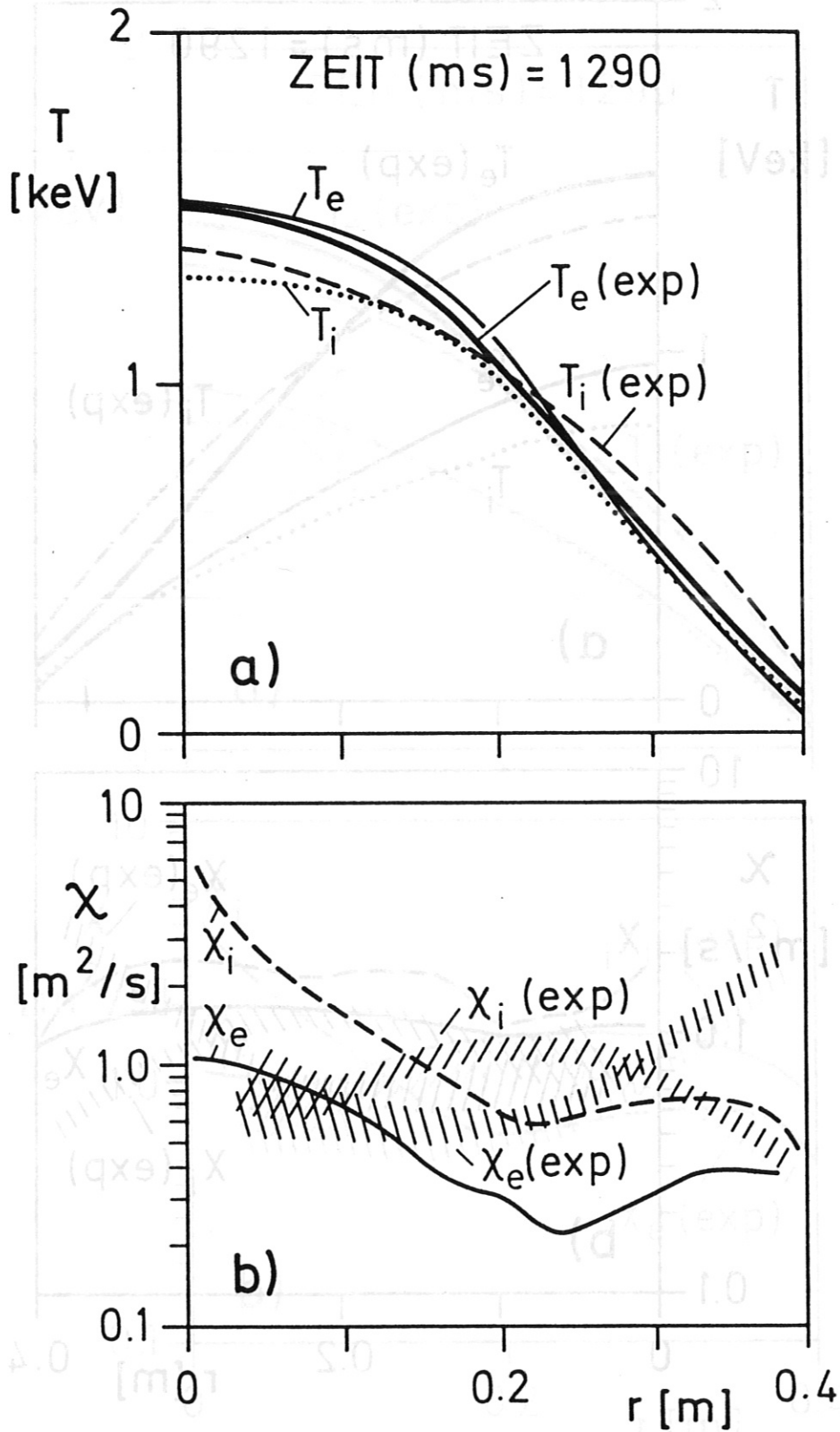
Fig.8 Radial profiles of measured (exp) and simulated electron and ion temperatures $T_{e,i}$ in the L-mode phase using χ_e from trapped electron mode driven transport theory (Appendix A-2/4,15/) and $\chi_i = 3\times \chi_{CH}$ (a). These electron and ion heat diffusivities $\chi_{i,e}$ are compared with the measured ones (exp) in (b).

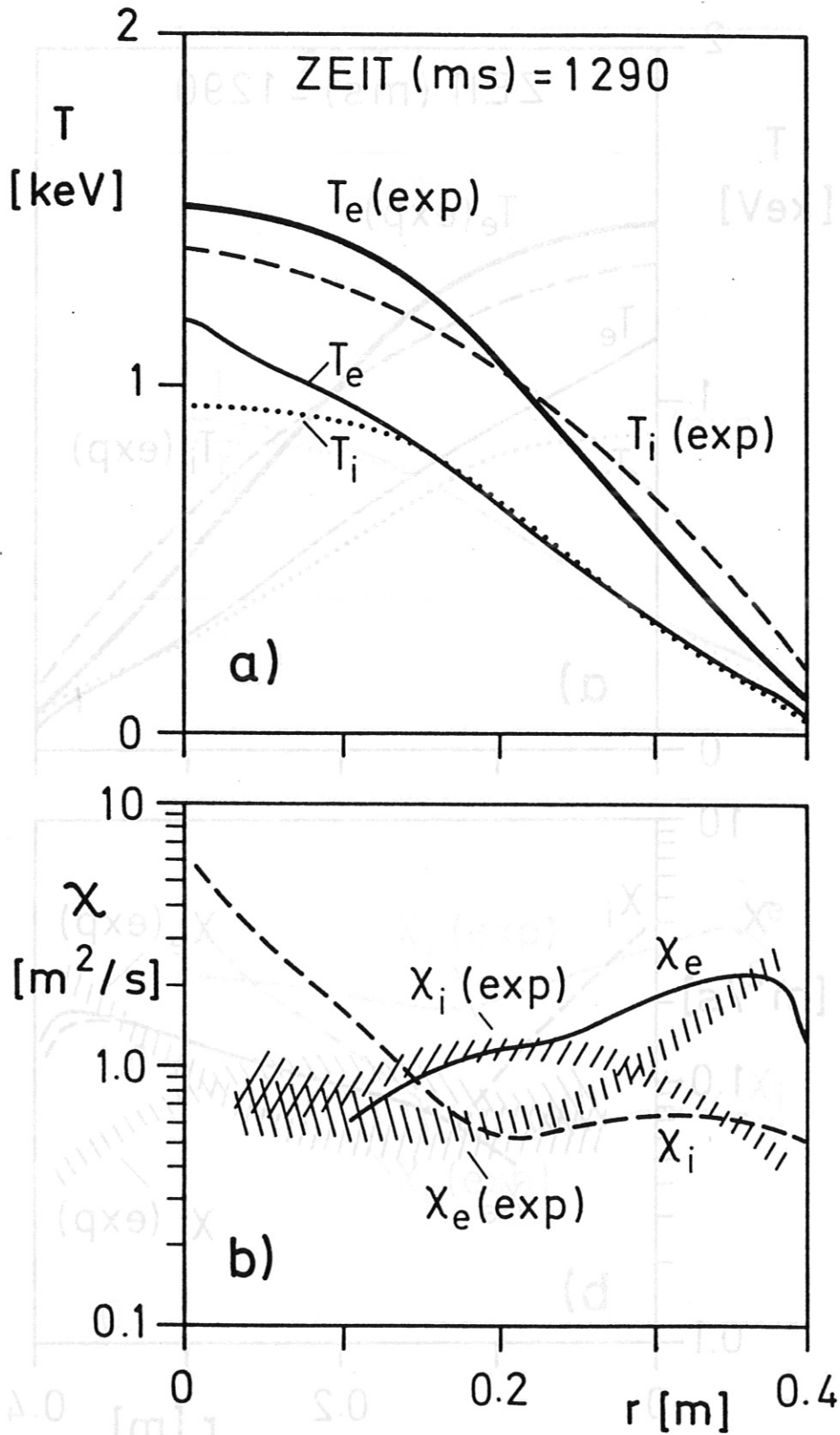Fig.9 Radial profiles of measured (exp) and simulated electron and ion temperatures $T_{e,i}$ in the L-mode phase using χ_e from trapped electron mode driven transport theory (Appendix A-2/4,15/) and χ_i from η_i mode driven transport (Appendix A-3-1 /4,13,15/) (a). These electron and ion heat diffusivities $\chi_{i,e}$, resp., are compared with the measured ones (exp) in (b).

Fig.10 Radial profiles of measured (exp) and simulated electron and ion temperatures $T_{e,i}$ in the L-mode phase using χ_e from trapped electron mode driven transport derived by A.Rogister(Appendix A-4 /10/) and $\chi_i = 3x \chi_{CH}$ (a). These electron and ion heat diffusivities $\chi_{i,e}$, resp., are compared with the measured ones (exp) in (b).
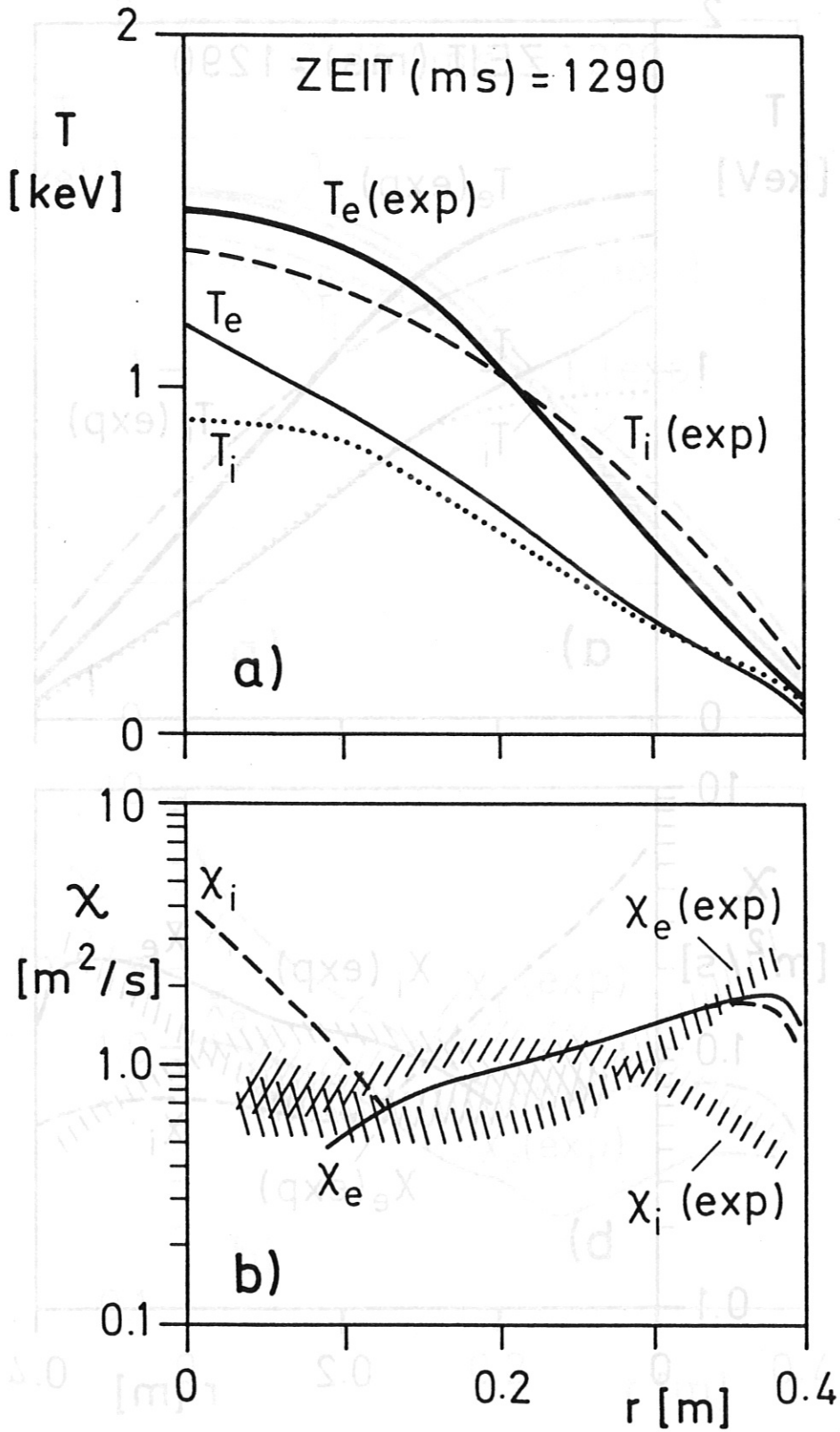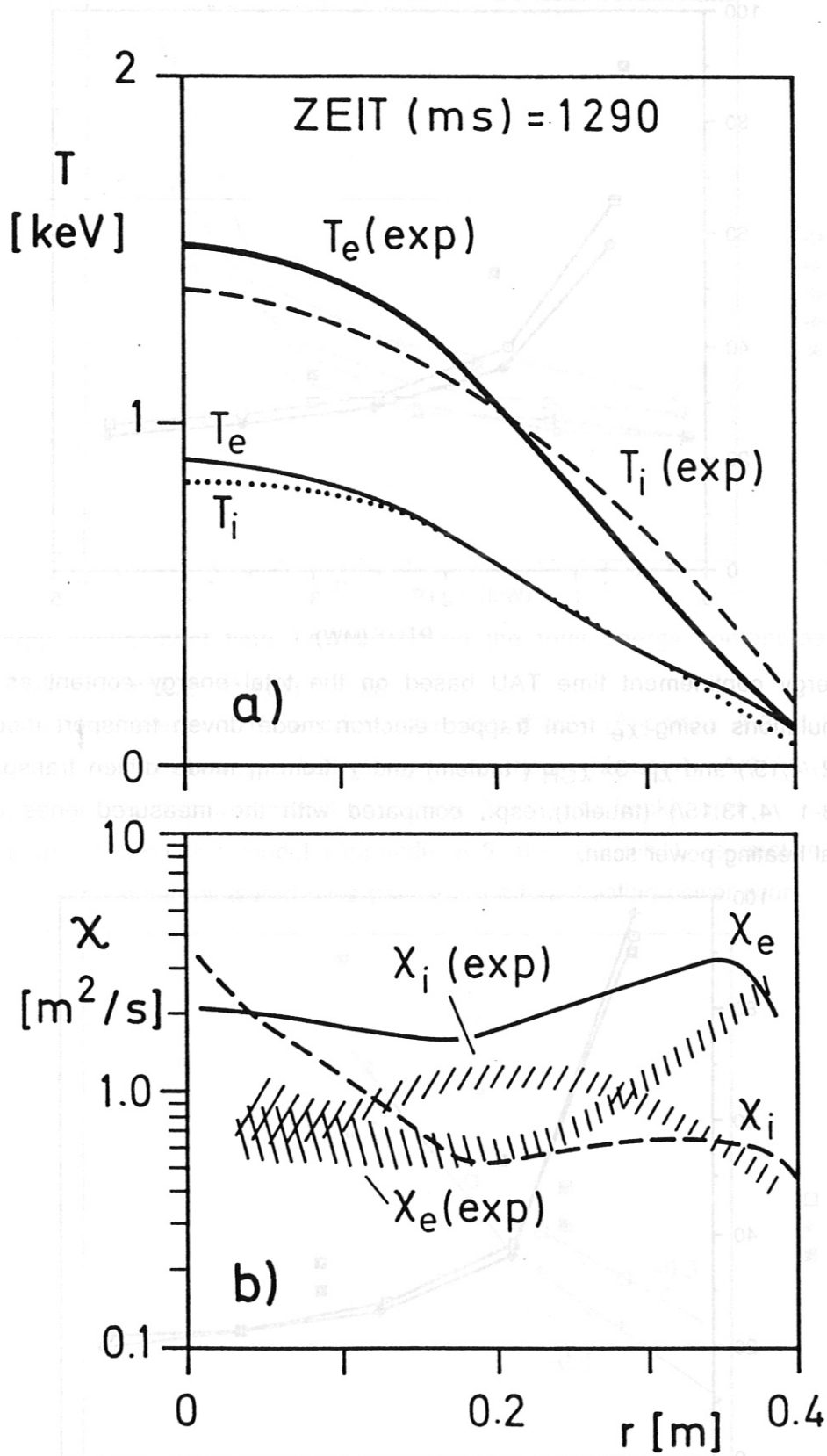
Fig.11 Radial profiles of measured (exp) and simulated electron and ion temperatures $T_{e,i}$ in the L-mode phase using χ_e from the Rebut-Lallia model (Appendix A-5 /6/) and $\chi_i = 3 \times \chi_{CH}$ (a). These electron and ion heat diffusivities $\chi_{i,e}$, resp., are compared with the measured ones (exp) in (b).

Fig.12 Radial profiles of measured (exp) and simulated electron and ion temperatures $T_{e,i}$ in the L-mode phase using χ_e and χ_i from the Rebut-Lallia model (Appendix A-5 /6/) (a). These electron and ion heat diffusivities $\chi_{i,e}$, resp., are compared with the measured ones (exp) in (b).

Fig.13 Radial profiles of measured (exp) and simulated electron and ion temperatures $T_{e,i}$ in the L-mode phase using χ_e from Becker's empirical model (Appendix A-6/9/) and $\chi_i = 3 \times \chi_{CH}$ (a). These electron and ion heat diffusivities $\chi_{i,e}$, resp., are compared with the measured ones (exp) in (b).
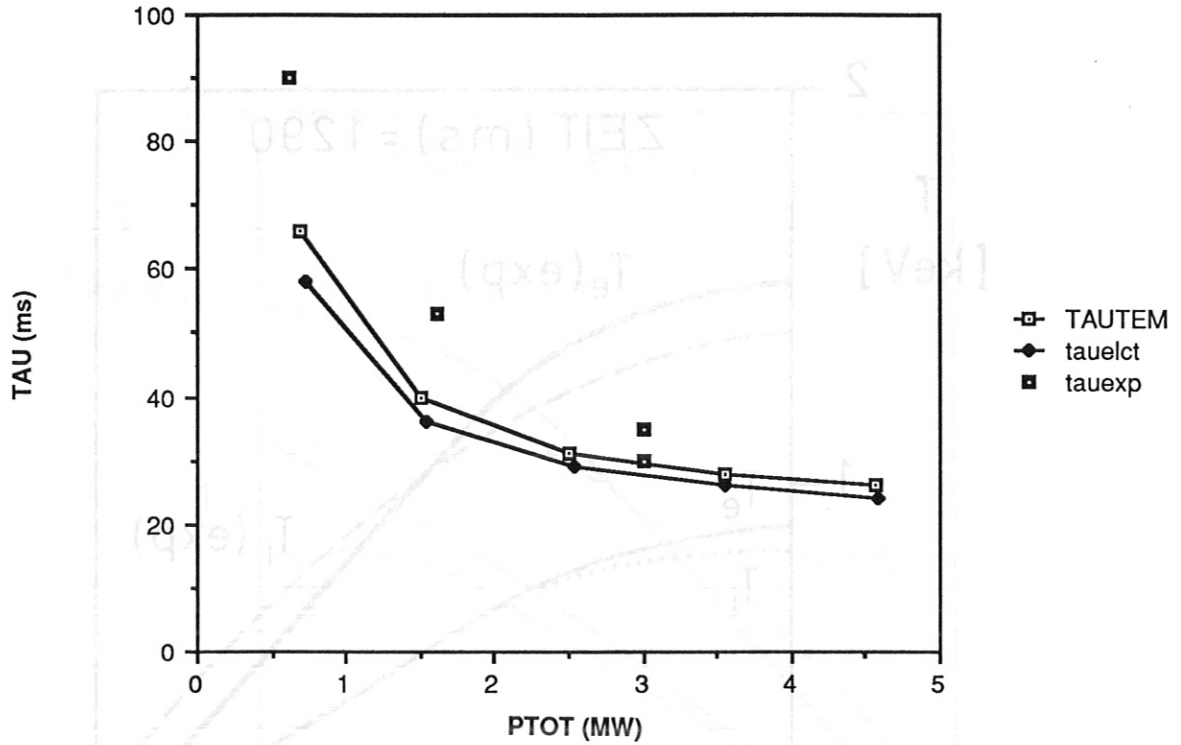
Fig.14 Energy confinement time TAU based on the total energy content as predicted by simulations using χ_e from trapped electron mode driven transport theory (Appendix A-2 /4,15/) and $\chi_i = 3 \times \chi_{CH}$ (tautem) and χ_i from η_i mode driven transport (Appendix A-3-1 /4,13,15/) (tauelct),resp., compared with the measured ones (tauexp) in a total heating power scan.
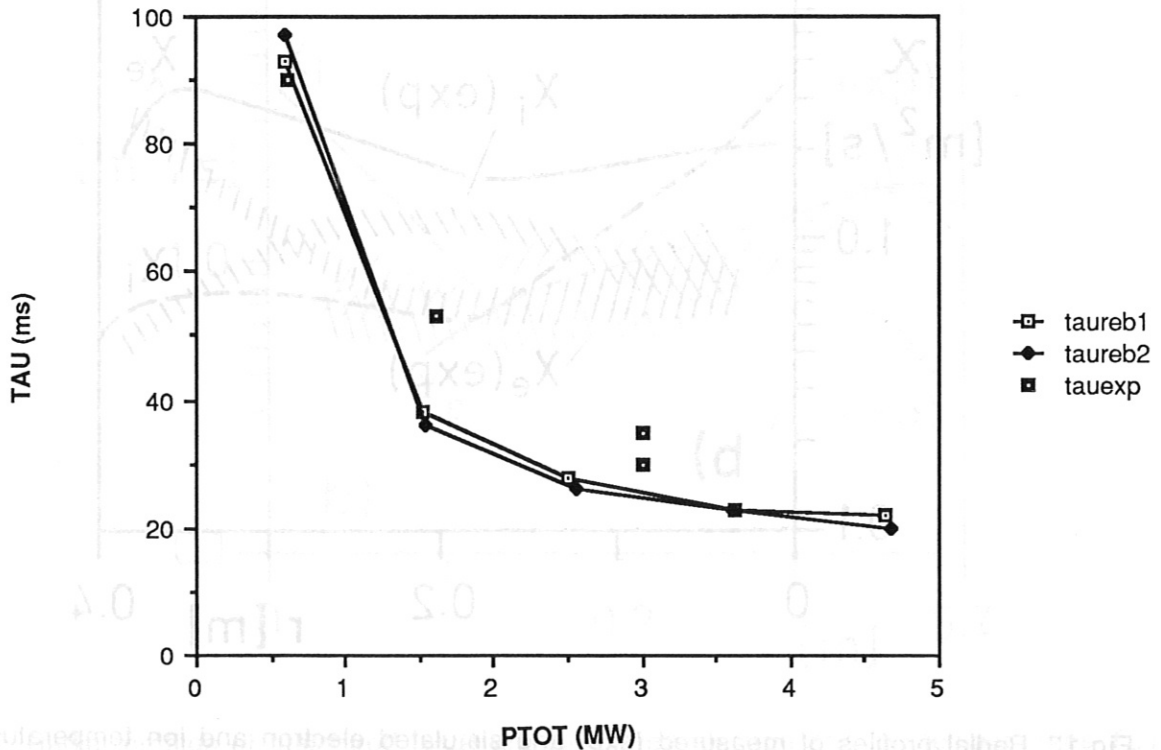

Fig.15 Energy confinement time TAU based on the total energy content as predicted by simulations using χ_e from the Rebut-Lallia model (Appendix A-5 /6/) and $\chi_i = 3 \times \chi_{CH}$ (taureb1) and χ_i from the Rebut-Lallia model (taureb2), resp., compared with the measured ones (tauexp) in a total heating power scan.
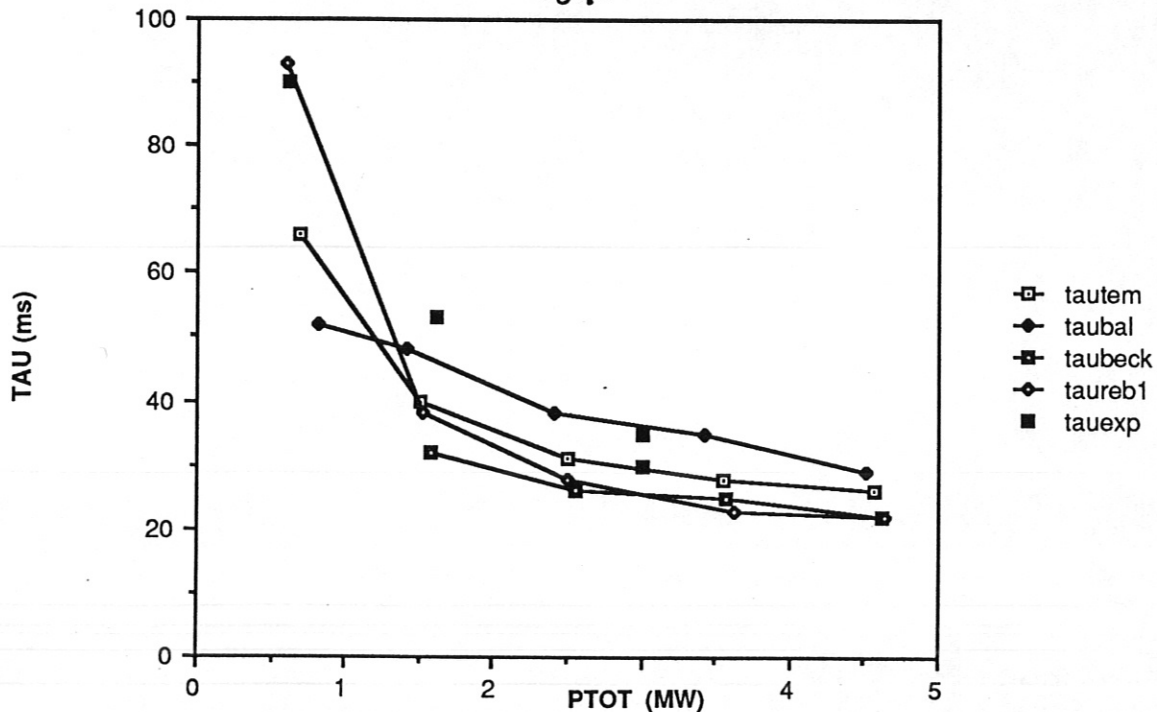
Fig.16 Energy confinement time TAU based on the total energy content as predicted by simulations using $\chi_i = 3 \times \chi_{CH}$ and χ_e

from trapped electron mode driven transport theory (Appendix A-2 /4,15/) (tautem),

from neoclassical resistive ballooning mode theory (Appendix A-1/7/) (taubal),

from Becker's empirical model (Appendix A-6/9/) (taubeck), and

from the Rebut-Lallia model (Appendix A-5 /6/) (taureb1), respectively, compared with the measured ones (tauexp) in a total heating power scan.
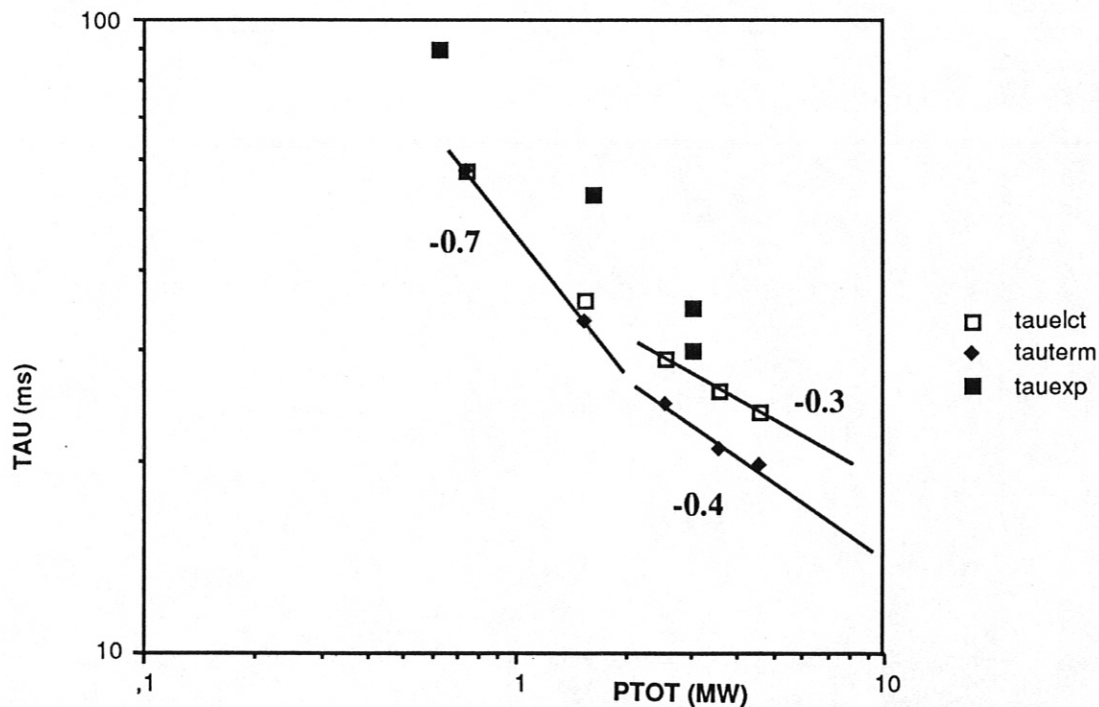

Fig.17 Energy confinement time TAU as predicted by simulations using χ_e from trapped electron mode driven transport (Appendix A-2 /4,15/) and χ_i from η_i mode driven transport (Appendix A-3-1 /4,13,15/) based on the total (tauelct) and thermal (tauterm) energy content, resp., compared with the measured ones (tauexp) in a total heating power scan.